

Article

# Stationary Battery Thermal Management: Analysis of Active Cooling Designs

Getu Hailu <sup>\*</sup>, Martin Henke and Todd Petersen 

College of Engineering, University of Alaska Anchorage, Anchorage, AK 99508, USA; mthenke@alaska.edu (M.H.); thpetersen@alaska.edu (T.P.)

\* Correspondence: ghailu@alaska.edu

**Abstract:** Stationary battery systems are becoming more prevalent around the world, with both the quantity and capacity of installations growing at the same time. Large battery installations and uninterruptible power supply can generate a significant amount of heat during operation; while this is widely understood, current thermal management methods have not kept up with the increase of stationary battery installations. Active cooling has long been the default approach of thermal management for stationary batteries; however, there is no academic research or comparative studies available for this technology. The present work presents assessment of different active cooling methods through an experimentally validated computational fluid dynamics simulation. Following model validation, several cooling system configurations were analyzed, including effects from implementing either a perforated vent plate or vortex generators. The vent plate was observed to greatly increase cooling performance while simultaneously promoting temperature uniformity between batteries. Vortex generators were shown to marginally increase cooling performance, yet, future research is recommended to study the effects and improvement of the design. The average battery temperature for the vented model is reduced by approximately 5.2 °C, while the average temperature differential among the batteries was only 2.7 °C, less than the recommend value (3 °C) by ASHRAE/IEEE Standards.

**Keywords:** battery; thermal management; lithium-ion; lead-acid; energy storage



**Citation:** Hailu, G.; Henke, M.; Petersen, T. Stationary Battery Thermal Management: Analysis of Active Cooling Designs. *Batteries* **2022**, *8*, 23. <https://doi.org/10.3390/batteries8030023>

Academic Editor: Torsten Brezesinski

Received: 6 January 2022

Accepted: 25 February 2022

Published: 1 March 2022

**Publisher's Note:** MDPI stays neutral with regard to jurisdictional claims in published maps and institutional affiliations.



**Copyright:** © 2022 by the authors. Licensee MDPI, Basel, Switzerland. This article is an open access article distributed under the terms and conditions of the Creative Commons Attribution (CC BY) license (<https://creativecommons.org/licenses/by/4.0/>).

## 1. Introduction

Stationary batteries generate heat under variety of conditions. Both the discharge and recharge cycles of operation can generate significant heat and, even when kept at a small float charge to prevent loss of power, there is a non-negligible amount of heat that is generated. In comparison to their smaller portable counterparts, stationary batteries do not have a comparable surface area to passively dissipate heat through natural convection and can reach unsafe temperatures quickly. Coupled with this fact, stationary battery systems may often work under volume constraints and be designed in such a manner that many batteries are contained within a small room or enclosure that is not conducive to heat removal. In the event that heat is not dissipated, high battery temperatures can lead to a reduced operational lifespan, sudden malfunction, and catastrophic failure. For these reasons, stationary battery systems often require accompanying thermal management systems to stay within acceptable operational temperatures. While it is accepted that thermal management is a necessary component in a stationary battery system, there has been little research into the development of new thermal management methods or the optimization and analysis of existing methods. Stationary batteries that operate at high temperatures suffer from a variety of negative consequences, including major safety problems in some circumstances. Thermal management that prioritizes safety while balancing expenses between the cooling system and battery degradation due to thermal impacts is referred to as optimal thermal management. However, this dynamic changes as stationary battery systems are further

implemented; high power Li-ion batteries become the dominant technology and power demands increase. Thus, it is worth investigating potential improvements in thermal management to ensure safe operation of stationary batteries while potentially lowering cooling costs.

## 2. Literature Review

A stationary battery is one that is used for energy storage and is kept in a fixed location. These batteries are further classified as either standby (i.e., batteries in an uninterruptible power supply) or cycling (i.e., batteries in a cycling system) (i.e., batteries comprising an energy storage system) [1]. In both cases, even if there are some differences, the fundamental principles are the same. Thermal management is an important consideration in the effective and safe operation of stationary batteries. While the harmful effects of high temperatures on batteries are widely established, most of the research has concentrated on applications for electric vehicles [2,3].

Energy storage is necessary in many applications including renewable energy sources, which are intermittent in their nature. Energy storage systems (ESS) are needed in order to establish a continuous, reliable and cost-effective power system [4–9]. Due to desirable properties, such as rapid discharge, modularity, and flexible scaling, battery energy storage systems (BESSs), which fall under the electrochemical division, have experienced tremendous investment and research [10–12].

Stability and continuous uptime are key aspects of system performance in modern electrical and data systems. The use of an uninterruptible power source to assure system stability is another application for stationary batteries (UPS). Power outages are expensive, with the majority of the expenses incurred in the industrial and service sectors in the form of lost income, materials, and labor disruption [13]. Telecommunications is particularly sensitive to brief power outages, as a power failure lasting as little as a second can result in long durations of service disruption as data centers resume [14]. These outages can be costly, and telecom operators may face contract penalties as a result [13,15]. These are also times when telecommunications are most wanted for emergency services, posing a public safety threat. All data centers are required to have a UPS in order to prioritize system uptime for public safety and minimize unplanned downtime. While a single server's battery installation may be tiny, the technology may be scaled up to hundreds of megawatts to run industrial processes while backup power is brought online [16–18]. Being scalable, modular, and a well-established technology, stationary batteries have long been the standard method for establishing a UPS.

### 2.1. Battery Heat Generation and Effects

Temperature rise is a known side effect of both charging and discharging processes in batteries, irrespective of the kind of battery. Uncontrolled heat generation can lead to safety issues and operational failure, as well as a significant reduction in the battery's operational expected lifespan or system failure [19–21]. A thermal management system is required to increase the functional lifetimes of batteries, reduce system maintenance, avoid system failure, and promote safety when operating at high temperatures.

Elevated temperature operation is a major factor in cell performance problems [22]. Batteries suffer from a variety of negative consequences at temperatures exceeding 50 °C, such as self-discharge, voltage drop, energy capacity decrease, and malfunction. The mean operating temperature of the battery is a significant factor in determining battery aging [23,24]. In general, each 10 °C rise in overall operating temperature above the recommended operating temperature reduces the lifetime of lead-acid batteries by half [14]. For Li-ion batteries, a 15 °C rise above the rated operating temperature results in a 50% decrease in lifetime [25,26].

Lead-acid batteries are still the mainstream technology for backup batteries. They should be stored between 20 and 25 degrees Celsius to avoid dramatic operating lifetime reduction. Maintaining operational temperatures of 20–25 °C for static batteries in hot envi-

ronments could be particularly difficult. As a result, there's been demand in using battery technologies that are best suited to higher operating temperatures. At temperature close to 35 °C, nickel–cadmium and lithium-based batteries show a reduction in life span, but this effect is far less significant than with lead-acid batteries [25]. Battery technology, outdoor environmental temperature, and electricity price play a role in the cost benefit analysis.

If the rate of heat generation in the battery is greater than the rate of cooling, the increase in temperature causes further rise in current and temperature, culminating in an unregulated current and temperature rise in a positive feed-back loop. This behavior is called thermal runaway; it can cause the battery to malfunction or melt [27,28]. While this phenomena can occur in any battery, big cells in use in static battery systems are particularly vulnerable to thermal runaway [29]. Li-ion cells possess combustible chemicals and are prone to thermal runaway, rendering the issue of particular concern to Li-ion system thermal control.

The minimization of temperature disparities among batteries is another element to consider in the thermal management of stationary battery systems. Temperature variations among batteries shorten life of the battery and raise the risk of failure. As per IEEE guidelines, the temperature difference between static batteries connected in series must not exceed 3 degrees Celsius [30].

## 2.2. Battery Thermal Management (BTM)

Although the need of thermal management for static batteries is obvious, there is presently a scarcity of studies on thermal management approaches for static batteries. The goals of thermal management systems, according to the IEEE/ASHRAE handbook for static battery thermal management (BTM), are to enhance performance of the battery while staying under budgetary restrictions and to guarantee optimum safety [27,28,31,32]. To achieve this goal, novel cooling methods are now being investigated and developed, including passive and free cooling, forced air, liquid cooling, phase change materials, and other ways [25,33–44]. The great bulk of work in creating innovative battery thermal management, on the other hand, are focused on battery packs for electric vehicles [2,45,46]. In spite of the variety of choices, passive air cooling systems continue to stay the industry norm for all battery cooling in data centers, and the only alternative discussed in IEEE/ASHRAE standards is an ambient passive cooling strategy customized to the thermal management of the room/enclosure instead of the individual batteries [27,28].

### 2.2.1. Air BTM Systems

Air cooling systems have a lot of advantages that make them the best choice for battery thermal control. Ventilation systems are well-understood, simple to implement and manage, and dependable as a technology. When properly implemented, air cooling systems are effective in heat removal, promoting temperature uniformity between batteries, and prevention of spot cooling single locations [47]. Spot cooling should be avoided since a difference in temperature inside a single cell might cause the battery to become electrically unbalanced and malfunction [27,28,48]. Another advantage of ventilation is that it eliminates the dangers of battery hydrogen gas evolution because air is mixed or vented into the surroundings [49]. Air cooling has long been the primary technique of BTM for static batteries due to its advantages and inexpensive prices [50]. Inexpensive and enhanced passive cooling systems have been demonstrated to be highly effective in minimizing the energy consumption required by a refrigeration cycle in studies [33,34,51]. This approach, nevertheless, is reliant on ideal outdoor weather conditions and necessitates the use of a regulated system. When comparing cooling options for static batteries, air cooling is often preferred over liquid cooling. Although liquid cooling systems provide superior cooling, they are more costly, complex, and prone to failure [47,52,53].

Bulk room ventilation is usually the most widely solution to BTM. Direct air cooling is not recommended because it can cause temperature disparities among batteries or spot cooling [53]. Spot cooling of an individual battery should be avoided because a difference in

temperature within a single cell might cause the battery to become electrically unbalanced and malfunction [27,28,48]. About 50% of lead-acid battery deployments utilize some form of thermal management method and about 30% monitor system temperature, according to a 2001 survey of utility and telecoms lead-acid battery installations. In southern climates, the usage of static battery deployments was likewise limited; thermal management problems are thought to be a major factor behind this tendency [54]. Batteries are frequently housed in enclosures, which is handy for being centrally located and securely confined. However, this necessitates for particularly strong thermal management to keep high temperatures to a minimum [55,56].

Adaptive thermal management of static batteries, while ubiquitous in portable batteries, has the potential to prolong battery life while reducing energy use by only delivering cooling when it is needed [57–59]. In order to facilitate cooling, these systems rely on reliable battery state readings with frequent sampling frequencies. Voltage, current, and battery surface temperature are the three battery states that can be constantly measured for a sealed cell [12,47,60,61]. This is a concern because the first two factors cannot always be utilized to predict heat generation because prediction models change as batteries age. Nevertheless, when properly designed, adaptive cooling can extend life of the battery and reduce energy consumption in big BTMs. Notwithstanding these benefits, insufficient information about the use of adaptive cooling in static batteries was discovered during this literature review.

### 2.2.2. Alternative Stationary BTM Systems

Liquid battery cooling systems have seen little advancement in their applicability to static systems, in spite of being a typical way of BTM for electric vehicles. By using pumped coolant to substantially boost the convective heat transfer coefficient and, hence, total convective cooling, liquid systems have been shown to be highly successful in cooling. Liquid convection BTM is by far the most prevalent approach of thermal management in electric vehicles, where fast discharge and substantial temperature rise are frequent operating characteristics. It has been effectively used in many electric vehicles to offer effective cooling [2,45,50]. Notwithstanding its excellent performance, liquid BTM has disadvantages, such as higher system complexity, maintenance, cost, and the possibility of leakage [62–64].

Phase change material (PCM) BTM systems, a new competitor, employ the latent heat during the phase change process of a substance to keep batteries at a fixed temperature [50,65]. Among the most appealing features of PCM systems is their ability to work passively, requiring no energy input during operation [66]. One of the disadvantages of PCM BTM is that it adds to the volume of the material. In circumstances of high heat generation, PCM may be restricted due to the phase change material's poor thermal diffusivity, which may limit the heat transfer response time. In the case of continuous cycling and heat generation, absorbed heat should eventually be dissipated from the PCM, which may necessitate the use of an additional cooling system [67]. There are issues about several typical PCMs' thermomechanical characteristics; more research into selection of materials and system design is ongoing [22,64]. Again, the majority of research has focused on mobile battery systems as the intended use; more work is needed to determine the practicality of PCM BTM strategies for high-capacity static batteries. Although active cooling has long been the default approach of thermal management for stationary batteries; however, there is no academic research or comparative studies available for this technology.

In particular, the present work contributes to the goal of improving cooling performance of a simple air-based, active cooling system in application to stationary batteries by

- developing several battery rack designs that could be used to increase cooling efficiency,
- investigating performance of each design under several metrics, including resulting battery temperatures,
- developing an experimentally validated computational fluid dynamics model for an active air-based battery cooling system,

- analyzing potential methods for improving air-based cooling system design and derive conclusions and recommendations that could guide future research and potential prototype design.

### 3. Materials and Methodology

Experimental and numerical approaches were utilized in this work. The experimental portion of research was done to provide validation of the numerical simulation. An experimental model has been constructed to represent a scaled-down version of a typical stationary battery rack that has been placed in an enclosure with attached ventilation and heat generation capabilities. Data collected from experimental trials were used in simulation as either independent driving variables or dependent outcome variables to be used in comparison with an identical simulation model. For example, measured variables such as inlet air speed were used as driving variables within the simulation. Battery temperatures measured from experimentation acted as the basis for comparison between the experimental and simulation models. The numerical simulation portion of research was used to investigate the performance of various cooling system designs. Using computational fluid dynamics (CFD) simulation, insight into the details such as temperature and velocity distributions were obtained.

#### 3.1. Model Design

The models used in both experimentation and simulation were meant to serve as a representative design of a typical stationary battery system. The default cooling design was created to reflect this; the experimental version of this model can be seen in Figure 1 with the assigned numerical values for each battery. The components of the model are sixteen batteries set on a two-level rack, placed inside an enclosure, with inlet duct and outlet air vent. Both the enclosure and the racks were of clear acrylic material, allowing the inside of the enclosure to be easily viewed during data collections trials.

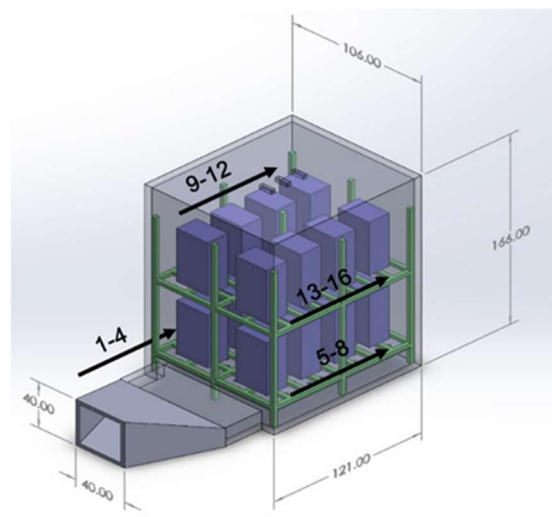


**Figure 1.** Model of the experimental design. The battery number assignments shown are consistent through all designs and models within this work. Dimensions are in millimeters.

The full-size model used in simulation is shown in Figure 2. Battery dimension and rack designs both of which were sourced from an existing stationary battery system design by C&D Technologies [68]. The resulting model can be seen below in Figure 2 and henceforth will be referred to as the “default” design.

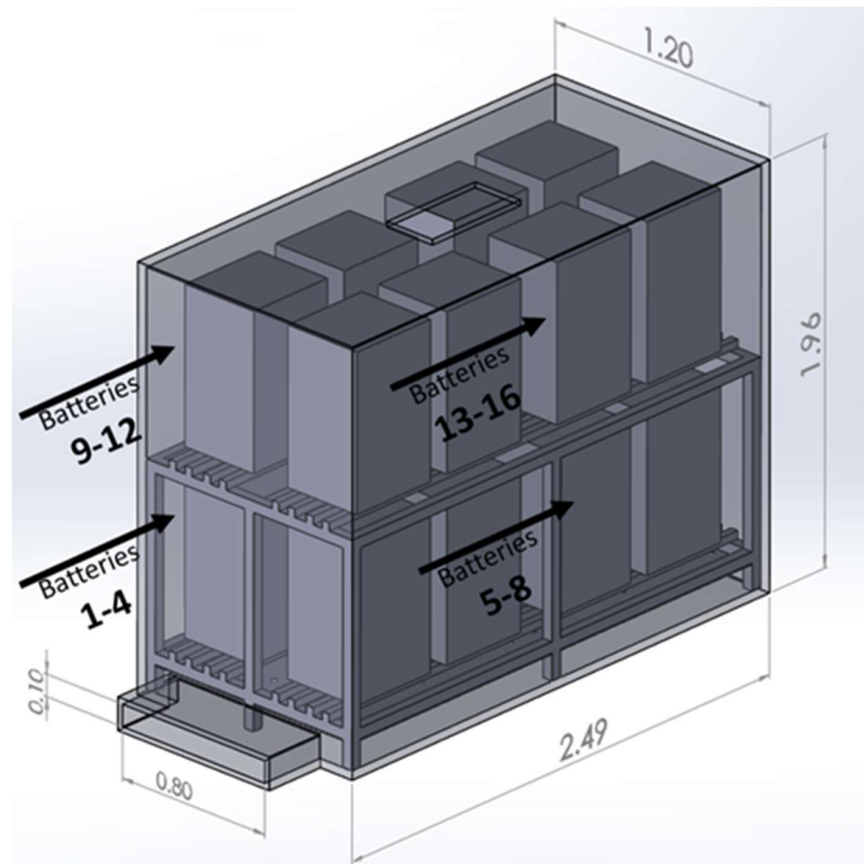


**Figure 2.** Full-scale default design model. All dimensions shown are in meters. Batteries grouping emulates the configurations typical of a stationary battery system.

Two additional alternative cooling designs were studied which consist of unique modular pieces that can be implemented onto the default design without changing the fundamental design. The first alternative was a perforated vent plate shown in Figure 3, which was attached to the bottom of the rack. The motivation behind the design was that the small perforations in the plate could create high velocity jets of air, thus, increasing the effective convective cooling. It was hypothesized that this design could also help in effectively distributing airflow throughout the entire enclosure, thus, reducing the incidence of temperature imbalances between batteries [69].

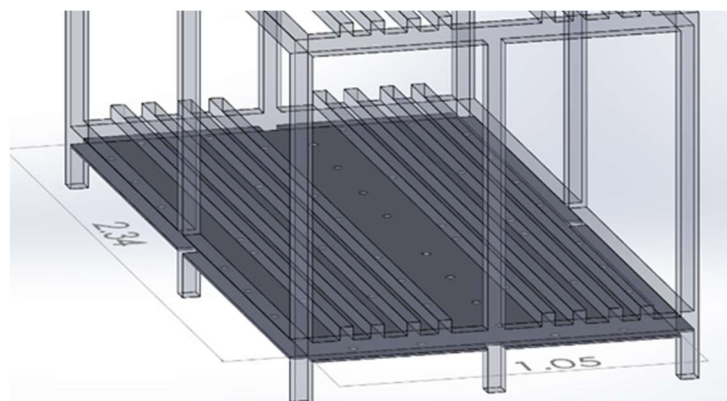


**Figure 3.** Vent plate attached to the bottom the rack. All perforations are circular and 3 mm in diameter. Dimensions are in meters.

The second design utilized small vortex generators attached to the rack as shown in Figure 4. Primary motivation behind this design lies in the ability of vortex generators to induce vortices and thus promote heat transfer by disrupting flow [70–72]. Disruptions in the fluid flow boundary layer can enhance convective heat transfer and vortex generators are used for this purpose to induce swirl flow [71]. A triangular delta wing type of vortex generator (shown in Figure 5) was selected for use within the model due to its simple geometry, which accommodates constraints on computational resources in simulation.

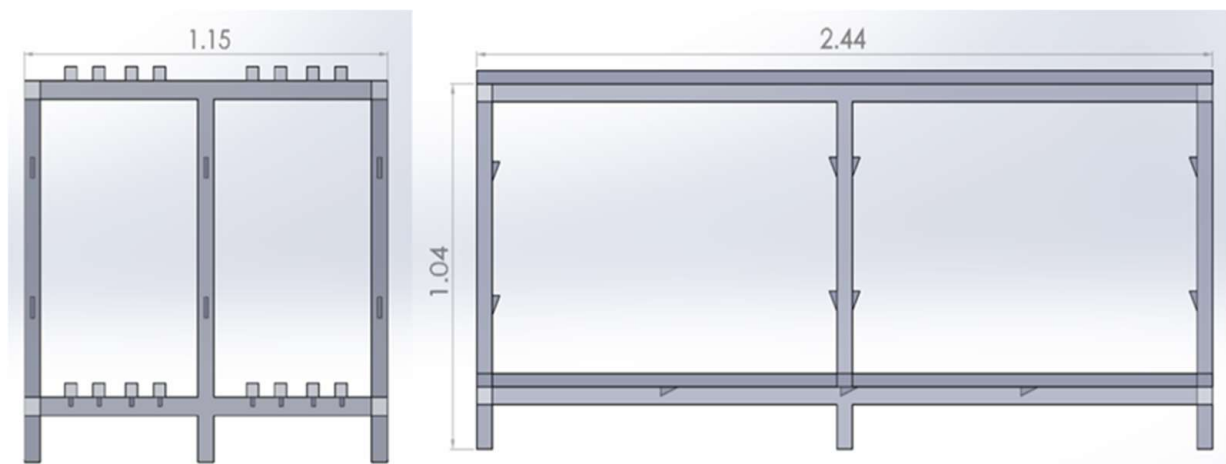


**Figure 4.** Front (left) and side (right) views of rack with vortex generators attached to bottom and vertical posts. Dimension shown are in meters.

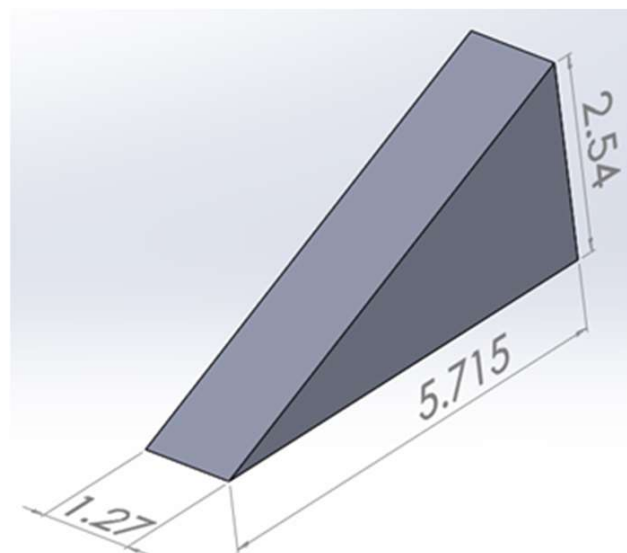


**Figure 5.** Triangular delta wing vortex generator mounted to rack within the vortex generator design model. Dimensions are in centimeters.

In summary, there were three distinct full-scale model designs analyzed through simulation.

- Default Model: 16 batteries placed on a rack contained within an enclosure with forced air vented underneath. This model is shown in Figure 2.
- Vented Model: Same construction as the default model besides the addition of a perforated plate to the bottom of the rack. This can be seen in Figure 3.

- Vortex Generator Model: Same construction as the default model besides the addition of small vortex generators to the underside and supporting arms of the rack. Attached vortex generators may be observed in Figure 4.

### 3.2. Experimental Model

A scaled-down battery testing apparatus was built to serve as a validation method for the numerical model. The experimental model was intended to represent a typical rack employed for stationary batteries. The enclosure design served as a simple model to establish a closed air space in which the effects of different cooling designs could be observed. While stationary batteries are often stored in specialized cabinets, the enclosure design was not sourced from a currently existing battery cabinet/cooling system. Rather, its intended function was to serve as the null condition and a method for defining the limits of the fluid domain. Two experimental models were constructed, one corresponding to the default cabinet design and the other corresponding to the vented model design. The design shown in Figure 6 uses sixteen rechargeable 9V Li-ion batteries connected in four parallel series, arranged on racks, and placed in an enclosure. The batteries were connected to six automotive 9006 halogen light bulbs used to create a resistive load allowing for battery discharge and heat generation to occur when the circuit was connected through a simple switch. The wiring diagram for the experimental design is presented in Figure 7. Air was forced through the inlet using a small  $40 \times 40$  mm fan (SoundOriginal, 8541605593) at a measured average velocity of 1.7 m/s.

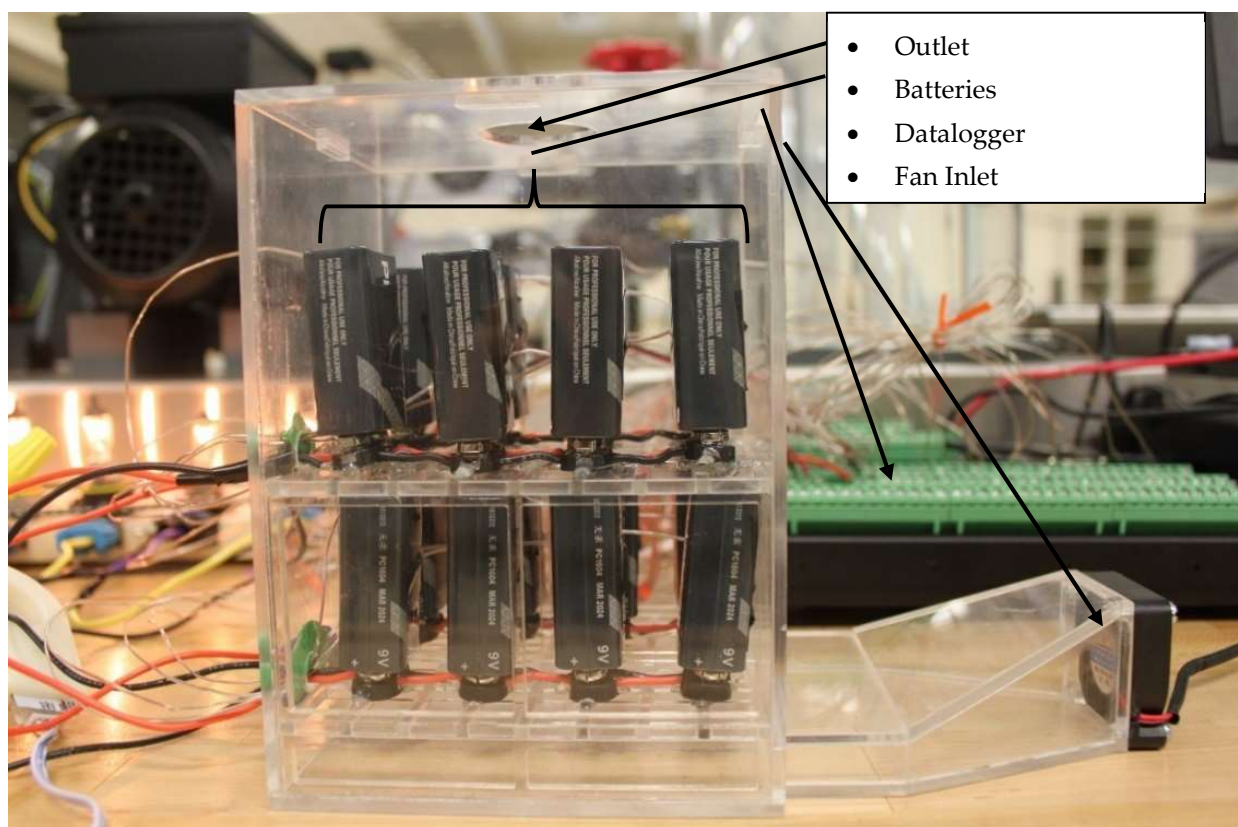


**Figure 6.** Data collection trial for the default model. Wires exiting through the backside of the case can be seen. Holes for wires/thermocouples were sealed with putty.

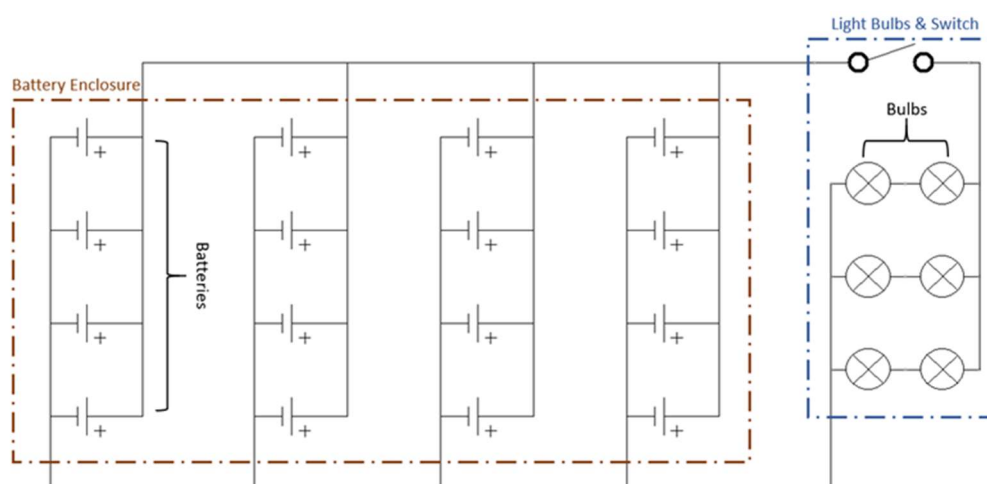


**Figure 7.** Wiring diagram for the batteries connected to a resistive load. Four parallel sets of four batteries are contained within the enclosure.

Data collection was performed, including inlet air velocity, ambient air temperature, battery temperature, and circuit current. In each data collection trial, all battery temperatures were monitored until an acceptable level of steady state was reached. Temperatures were monitored by thermocouples attached to AM16/32B Channel Multiplexer. The datalogger and multiplexer were powered by a Campbell Scientific PS100 external battery. All thermocouples used were type K, capable of measuring temperatures up to 105 °C. Battery temperatures were sampled every 30 s by the datalogger; the data were sent and compiled in an accompanying computer using PC400 Datalogger Support Software. Inlet air speed and temperature were measured using Extech Anemometer (with accuracy of  $\pm(3\% + 1 \text{ d})$  of reading). Battery voltage and internal resistance were measured using Klein Tools clamp meter; circuit current was continually monitored by the Bayit Ammeter (with accuracy of  $\pm 0.01$ ). In simulation, these recorded variables were used to specify air inlet flow parameters and model the approximate heat generation for all batteries.

The batteries used in the experiments were Duracell Procell 9V alkaline batteries. These batteries were chosen as they were capable of functioning safely up to 54 °C and could be bought in bulk for testing. Before being installed into the circuit, each battery was tested using the Klein CL200 clamp meter to insure uniform voltage for all cells in use. The instruments used in data collection and the variables quantities measured are summarized in Table 1 below.

**Table 1.** Instruments paired with variables measured within the data collection process.

Manufacturer	Instrument	Quantity Measured
EXTECH	40711 Hot Wire Thermo-Anemometer	Airflow Velocity
CAMPBELL SCIENTIFIC	Cr1000 × Datalogger	Battery Temperatures
CAMPBELL SCIENTIFIC	AM16/32b Channel Multiplexer	Battery Temperatures
CAMPBELL SCIENTIFIC	PS100 External Battery	Battery Temperatures
KLEIN TOOLS	600A Clamp Meter CL200	Battery Voltage
BAYIT	DC 5–120 V 100 A Mini Digital Current Ammeter	Circuit Current
OMEGA	5TC-TT-K-30-72	Battery Temperatures

### 3.3. CFD Simulation

Simulation was performed using Ansys Fluent 19.2 software with an imported model created using Solidworks 2018 software. For the simulation a steady state was assumed. As energy storage systems and uninterruptible power supplies are expected to provide constant power on a time scale of hours, this was expected to be an acceptable assumption. In operation over long periods of time, it was assumed that batteries reach a steady state temperature, as heat generation and removal are eventually balanced. Furthermore, preliminary simulations have not shown the presence of bulk transient effects in the fluid dynamics, thus, indicating steady state could be used to accurately describe the flow.

The fluid domain and batteries were both modeled with thermal properties, while the rack and enclosure were treated as adiabatic materials so that only heat removal directly from the battery surface via forced and natural convection was considered. A tetrahedral mesh was created for the fluid domain, with localized refinement and inflation layers placed in order to properly resolve boundary layers. A mesh sensitivity study was performed for the experimental and full-size model to identify optimal mesh size for accurate results. Figure 8 below shows the experimental model mesh sensitivity analysis performed by sampling the inlet air speed profile underneath the rack from the front of the case to the opposite side. The coarse mesh consists of 2.5 million elements, the medium mesh has 6 million; the fine mesh contains 12 million elements. While no mesh fully diverges, it can be seen in Figure 8 that the coarse mesh does capture the decline in velocity, just as the medium or fine mesh. The medium mesh only diverges slightly approaching the wall. Thus, the medium mesh was used for experimental simulations in order to conserve computational resources.

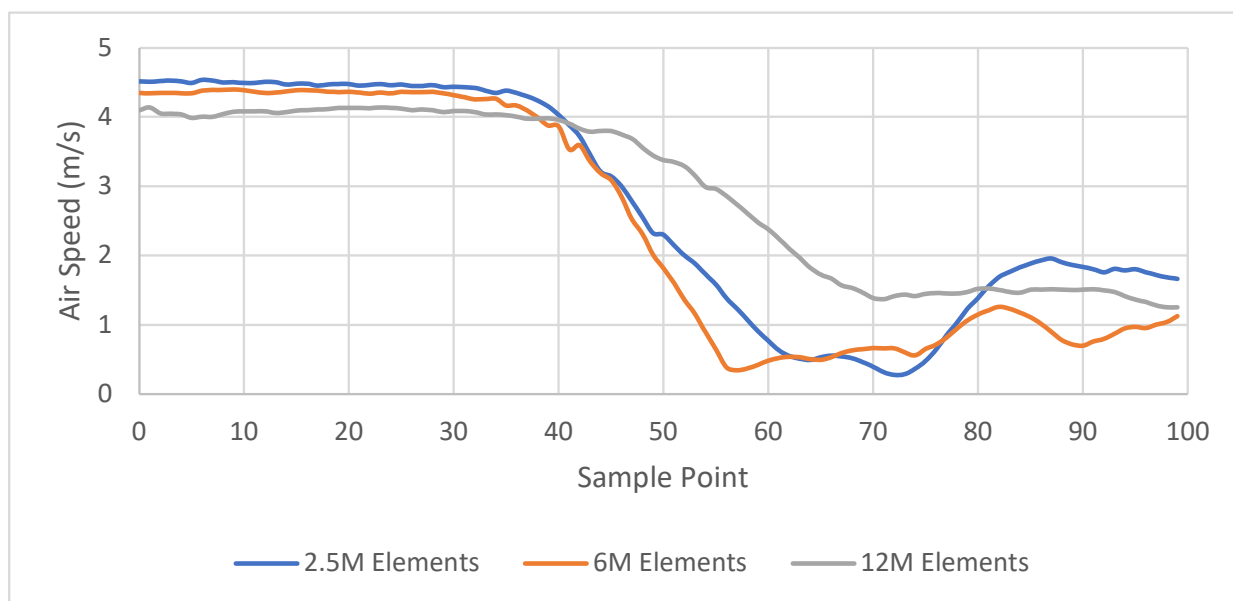


**Figure 8.** Mesh sensitivity analysis performed for the experimental model using a fine, medium, and coarse mesh containing 12, 6 and 2.5 million elements, respectively. The parameter measured for analysis is air speed sampled in a line underneath the rack in the direction of inlet flow.

To prevent error attributed to changes in model meshing, the default element sizes between all models were specified to be the same. The only exceptions to this condition occurred where mesh refinement was done at the vent plate perforations and near vortex generator geometry. In order to capture the complex geometry present between different models, the meshing method used primarily tetrahedral elements for the fluid domain. Mesh inflation layers were implemented near fluid inlet and outlets as well as at the interface between batteries and fluid. In effect, the use of inflation layers should lead to better boundary layer flow simulation and improved heat transfer prediction. The resulting

mesh used for experimental simulation can be seen below in Figure 9 where a section plane has been applied to show the internal fluid mesh and batteries contained within.

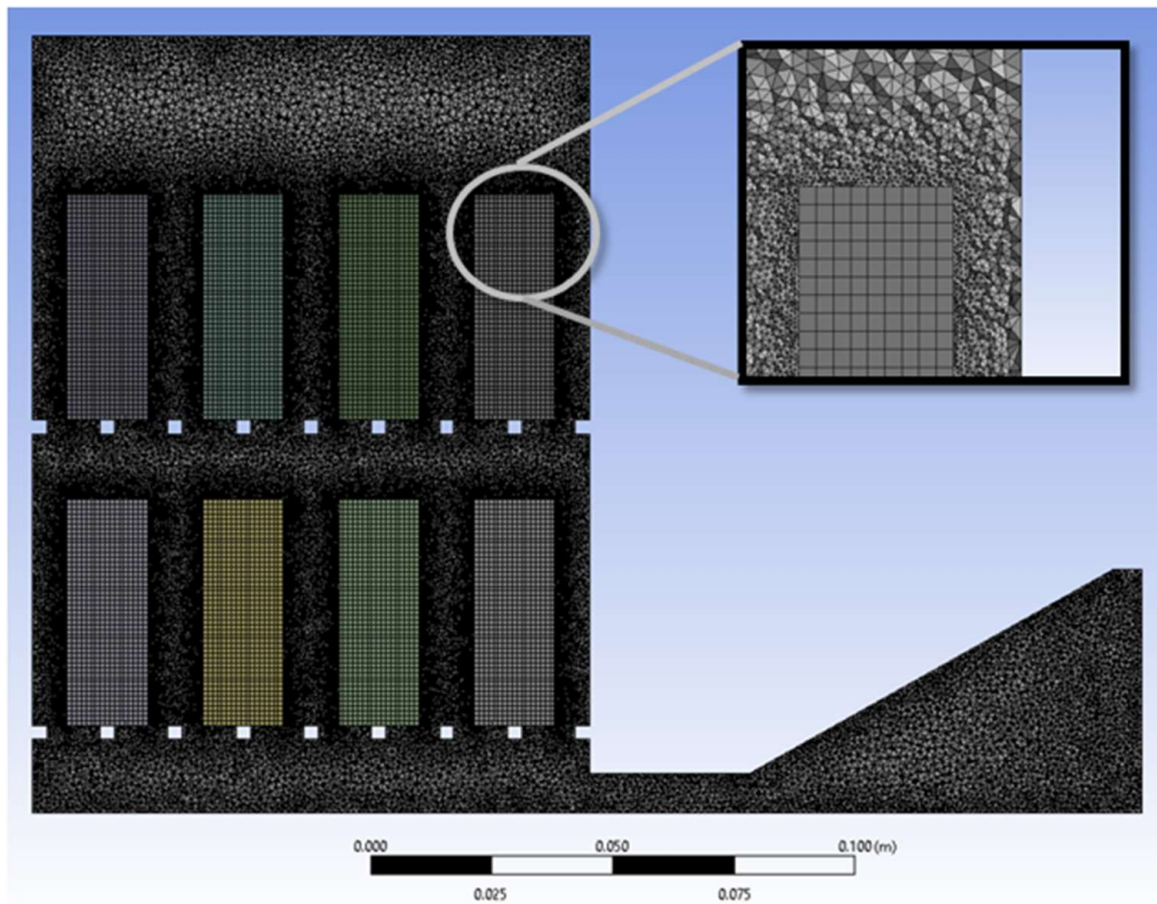


**Figure 9.** Mesh domain used in simulation of the experimental model. A section plane operation has been applied to show in the internal fluid domain and the batteries contained within. In addition, an enlarged 3D rendering of the mesh surrounding the corner of a single battery can be seen in the top right corner of the figure.

Governing equations used include the mass, momentum, and energy conservation equations shown below through Equations (1)–(5). The dissipation function  $\Phi$  in the energy equation is negligible as it represents the conversion of mechanical energy within the fluid to heat, a physical process significant in high velocity or viscous flow, which does not apply in this application.

Mass:

$$\frac{\partial \rho}{\partial t} + \nabla \cdot (\rho \mathbf{V}) = 0 \quad (1)$$

Momentum ( $x, y, z$  directions in order):

$$\frac{\partial \rho u}{\partial t} + \nabla \cdot (\rho u \vec{V}) = -\frac{\partial P}{\partial x} + \nabla \cdot (\mu \nabla u) + \rho f_x \quad (2)$$

$$\frac{\partial \rho v}{\partial t} + \nabla \cdot (\rho v \vec{V}) = -\frac{\partial P}{\partial y} + \nabla \cdot (\mu \nabla v) + \rho f_y \quad (3)$$

$$\frac{\partial \rho w}{\partial t} + \nabla \cdot (\rho w \vec{V}) = -\frac{\partial P}{\partial z} + \nabla \cdot (\mu \nabla w) + \rho f_z \quad (4)$$

Energy:

$$\frac{\partial \rho}{\partial t} + \nabla \cdot (\rho \vec{V}) = -p \nabla \cdot \vec{V} + \nabla \cdot (k \nabla T) + \Phi + S_i \quad (5)$$

where

$k$ —Thermal Conductivity

$t$ —Time

$u$ —x-velocity

$V$ —velocity vector

$v$ —y-velocity

$w$ —z-velocity

$\mu$ —Viscosity

$p$ —Pressure

$\Phi$ —Dissipation Function

$S_i$ —Energy source

$T$ —Temperature

$\rho$ —density

As the model has instances of flow disruptions, complex geometry, and high velocity, turbulence will be present within the model. The Reynolds number at the inlet duct for the experimental model was calculated to be 4100. Because this number lies in the transitional region between laminar and turbulent flow, laminar flow could not be assumed. For this reason, a turbulence model was selected to provide accurate prediction. The turbulence model selected for use in the simulation was the  $k$ - $\omega$  shear stress transport (SST) model. Through the literature review, this turbulence model was found to be best suited to predict the fluid behavior and heat transfer [69,72–77].

The SST model combines two equations for turbulence modeling by incorporating the  $k$ - $\epsilon$  turbulence model for far field simulation and the  $k$ - $\omega$  turbulence model for the boundary layer in near-wall prediction [72,74]. In a recent study assessing the ability of different turbulence models to simulate duct flow behavior and heat transfer, the SST model was found to have less than 1% error in prediction of total heat transfer [75]. Furthermore, the SST model has been demonstrated experimentally to accurately describe the flow of air through perforated plates similar to the vent plate used in the alternate system designed in this research [69]. In summary, the SST model has been demonstrated to have the ability to accurately simulate flow separation and near wall behavior, while maintaining accurate prediction of flow in shear free regions, thus, making it the ideal turbulence model to accurately simulate heat transfer for the model [72,76,77].

A lumped capacitance model was employed, in which a simplifying assumption was made that temperature within the batteries is spatially uniform; thus, thermal properties of the battery are spatially uniform. This model has been used successfully in prediction of battery thermal behavior in other studies [78,79]. The Biot number ( $Bi$ ), which is the ratio of the convective heat transfer at a solid body's boundary to conductive heat transfer within the body, was used to identify whether the lumped capacitance model was appropriate (Equation (6)). Here,  $h$  represents the convective heat transfer coefficient,  $L_c$  is the characteristic length (volume divided by surface area) of the battery, and  $k$  is the internal thermal conductivity of the battery.

$$\frac{L_c h}{k} = Bi \quad (6)$$

$Bi < 0.1$  is seen as an acceptable threshold for application of lumped capacitance [78,80]. Ultimately, the application of a lumped capacitance model was deemed appropriate for the experimental simulation and the details are given in the following section.

### 3.4. Experimental Model Simulation

For an individual 9V battery,  $L_c$  was found to be approximately 0.005 m. Effective thermal conductivity values have been reported to range from 2 to 3 W/m-K [81,82].

Utilizing these values in Equation (1) shows that the lumped capacitance model is expected to be appropriate up to effective convective heat transfer coefficient values of approximately  $40 \text{ W/m}^2\text{-K}$ . From initial simulations, surface heat transfer coefficients were not seen to exceed  $25 \text{ W/m}^2\text{-K}$  for a range of different input parameters realistic to the airflow seen in the experimental model. For this reason, it was assumed that a lumped capacitance model was justified for use in the experimental mode simulation.

Acceptable values for specific heat capacity for sealed lead-acid batteries range between  $0.7$  and  $0.9 \text{ kJ/kg-K}$  and value of  $0.8$  was selected to represent the average of this interval [83,84]. For the heat generation variable, a volumetric-based heat model was used. In calculating the magnitude of this variable, only heat evolution due to resistive effects within the battery was accounted for [85,86]. During discharge, there was a cooling effect due to entropy change in the battery, but this is small compared to the heat generation due to Ohmic heating during high discharge rates within lead-acid batteries. Another simplifying assumption pertaining to the battery thermal model was that heat generation was uniform and constant between all batteries. Input variables used within the validation simulation can be found compiled in Table 2.

**Table 2.** Input variables used within experimental model simulation. Variables pertaining to air flow were measured from experimental model trials.

Variable	Value	Unit
Battery-Specific Heat Capacity	800	J/kg-K
Battery Conductivity	250	W/m-K
Inlet Air Temperature	22	°C
Inlet Air Velocity	1.7	m/s

### 3.5. Full-Scale Simulation

As previously described, the design of the full-scale model differs slightly (rack geometry differs, batteries have less space, battery dimensions are altered) in order to remain similar to the validated experimental model while accurately representing existing battery installations. Many heat transfer analysis validation studies allow for some deviation between CFD simulation and the associated experimental validation [87–89]. In this case, agreement between experimental and full-scale models was thought to be acceptable, as the overall design of both models remained similar and the rack design was simplified for the full-scale model. The scale of analysis had changed drastically with the dimensions of the enclosure exceeding two meters. The batteries modeled within the enclosure had the geometry, size, and thermal characteristics of lead-acid batteries, such as those used in the uninterruptible power supplies. This change in battery technology was considered an allowable change as a lumped capacitance model was used and, while battery temperatures were used to compare cooling performance, the battery response to temperature change was not simulated.

Quantities selected for the simulation were meant to be representative of common operational conditions for a stationary battery system. The selection of boundary conditions and material properties used in simulation was done with emphasis on being representative of typical system parameters. Battery-specific heat capacity of flooded lead acid batteries was reported through literature to be slightly over  $1000 \text{ J/kg-K}$  and thus this value was selected as a reasonable approximation [83]. Inlet air flowrate was set at  $400 \text{ cfm}$  which could be easily achieved through an  $8''$  duct fan. This value was chosen after performing several initial simulations to deduce the approximate amount of inlet air that would lead to similar temperature regimes as experienced in experiments and thus adhere to the validation established through the experimental model. Heat generation was calculated assuming a medium rate of discharge (relative to battery capacity) for a lead acid battery used in an uninterruptible power system. Assuming resistive heating to be the only source of heat generation and using the internal resistance given through a stationary battery

spec sheet, the volumetric heat generation was estimated to be 75 Watts per battery. All parameters defined in the full-scale simulation are listed in Table 3.

**Table 3.** Input variables used within full-scale model simulation.

Variable	Value	Unit
Heat Generation per Battery	75	Watts
Battery-Specific Heat Capacity	1000	J/kg-K
Battery Conductivity	250	W/m-K
Inlet Air Temperature	22	°C
Inlet Air Flowrate	400	cfm

Simulation of different cooling configurations with identical input variables allowed for efficacy of each design to be assessed by analyzing battery temperatures. Following this study, individual parameters such as airflow were altered to analyze the effects and to establish a comparative study for cooling performances.

In addition, variables such as the surface Nusselt number ( $Nu$ ) were derived to demonstrate the relationship between fluid motion, heat transfer and resulting battery temperature.

Normally a difficult value to measure, CFD allows Nusselt number ( $Nu$ ) to easily be sampled. This was done using the heat flux at each element face on the fluid-solid boundary  $q_p$ , calculating the temperature difference between the battery surface ( $T_p$ ) and fluid temperature, and using the distance  $x_p$  as the distance from the surface leading edge to point of analysis. Equation (7) shows how this is done by making a substitution for the convective coefficient.

$$Nu = \frac{q_p x_p}{(T_p - T_f)k} \quad (7)$$

where

$Nu$  is Nusselt number

$q$  is heat flux

$T$  is temperature and

$K$  is thermal conductivity

## 4. Simulation Validation

### 4.1. Simulation Validation

For the validity of the CFD simulation to be established, experimental trials were performed on default and vented designs to serve as a comparison to simulation output. The battery temperature profiles can be seen in Figure 10 for the default design and Figure 11 for the vented model. In both cases, batteries were continuously discharged until a steady state temperature was reached. These temperatures were compared with the simulation temperature to evaluate the validity of the CFD simulation and to justify its use in the analysis for the full-size model.

For the experimental default model, the current through each branch was found to be 1.1 amperes on average, which was used to calculate the resistive heating as 1.17 watts per battery, according to an internal resistance value measured to be 0.97 ohms. For the experimental vented design, the average current was measured to be 1.6 amperes with a measured internal resistance of 0.83 ohms. This difference in current between the two cases results in different heat generation according to the thermal model and each simulation has been adjusted to reflect this difference.

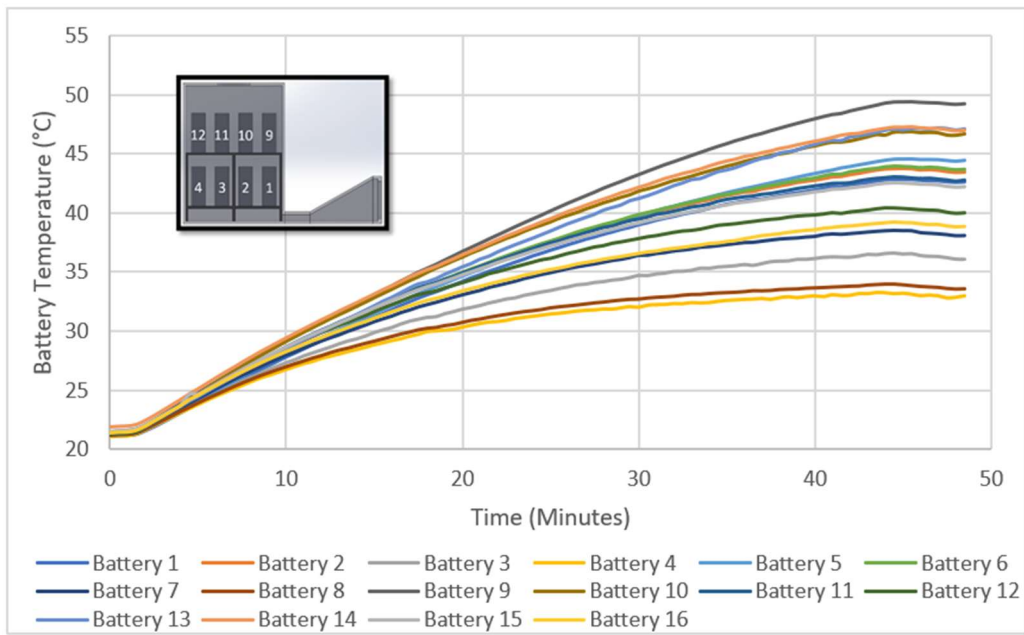


**Figure 10.** Default model battery temperatures. Batteries near the front of the enclosure have higher temperatures while batteries opposite the inlet experience lower temperatures.

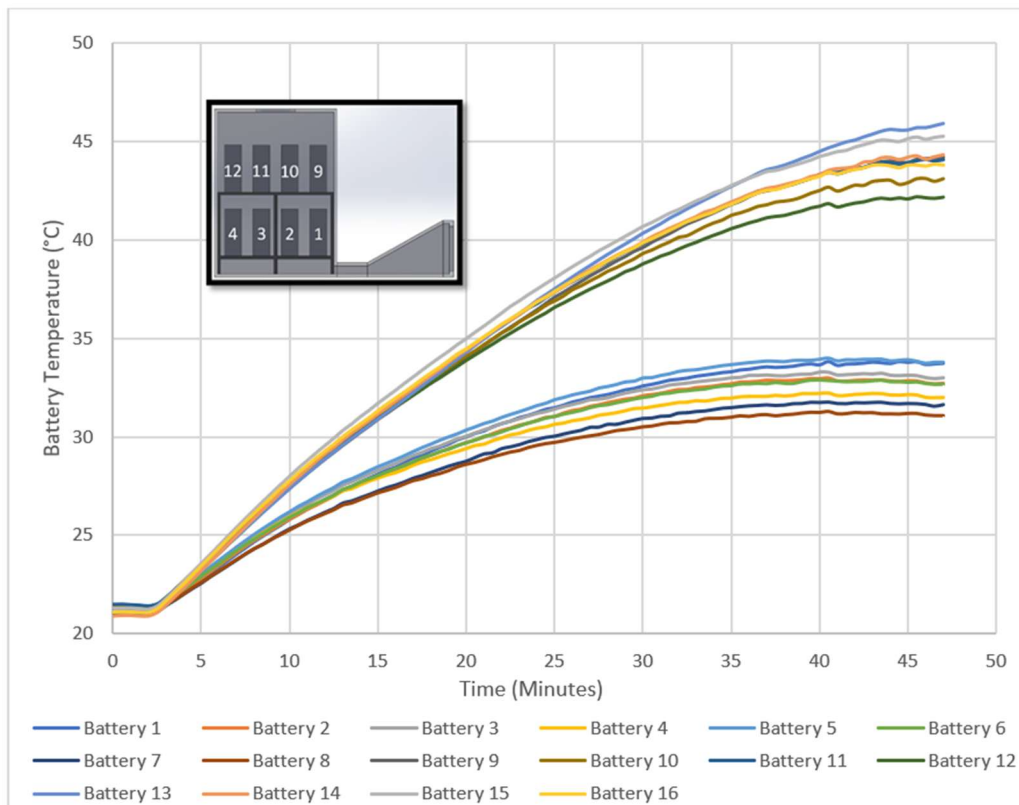


**Figure 11.** Vent model battery temperatures. The two large groupings reflect batteries placed on either level of the rack. The lower temperatures belong to batteries on the bottom level of the rack and the elevated temperatures belong to batteries on the top level.

Noticeable differences were observed in battery temperatures when comparing Figures 10 and 11. The vented model showed a clear division between battery temperatures for the upper and lower rack levels. All batteries on the lower level had substantially

lower temperatures; the proximity to the vent plate and associated jets of air is thought to be the driving factor behind this trend.

When observing the battery temperature profiles shown in the above figures, there is a point at which battery temperatures cease to rise and become steady. These temperatures form the comparison basis for the simulation validation study. The identical simulation model uses the measured air flow and heat generation variables to drive the CFD simulation. The fluid flow present in the default design obtained from the CFD analysis can be seen below in Figure 12. From Figure 12, it is seen the fluid accelerated to the back, and batteries at the back on the lower rack were cooled better. The temperatures for the experimental and simulation default and vented models have been compiled in Tables 4 and 5.

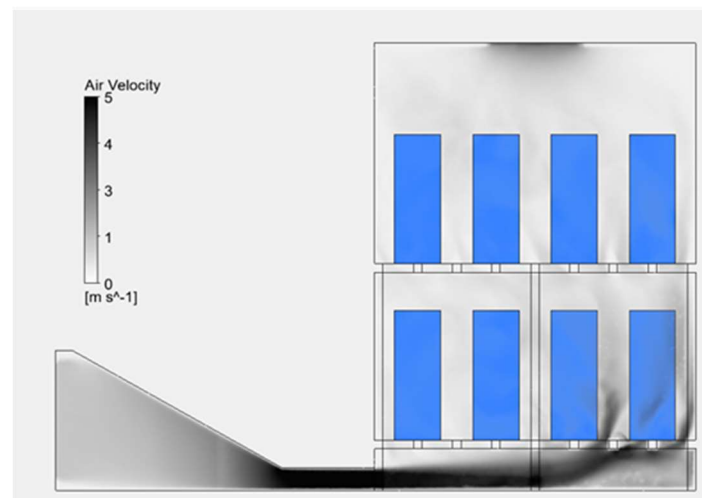


**Figure 12.** Volumetric representation of air flowing through the default experimental model in simulation.

**Table 4.** Default design experimental and simulation temperature comparison.

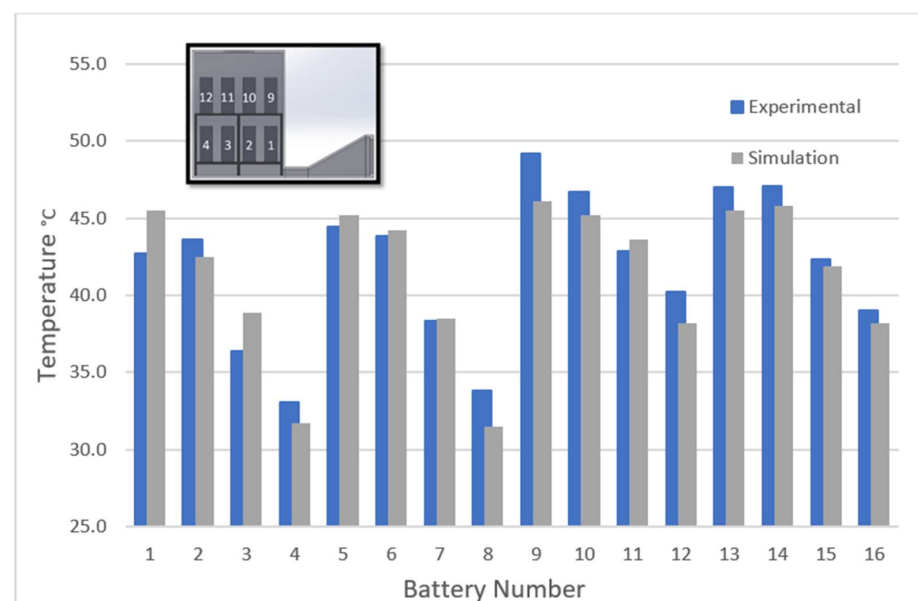
Battery	Default Experimental Model Steady State Temp °C	Default Simulation Model Temp °C	Absolute Error Temp °C
1	42.7	45.5	2.8
2	43.6	42.5	1.1
3	36.4	38.9	2.5
4	33.1	31.7	1.4
5	44.4	45.2	0.8
6	43.8	44.2	0.4
7	38.3	38.5	0.2
8	33.8	31.5	2.3
9	49.2	46.1	3.1
10	46.7	45.2	1.5
11	42.9	43.6	0.7
12	40.2	38.2	2.0
13	47.0	45.5	1.5
14	47.1	45.8	1.3
15	42.3	41.9	0.4
16	39.1	38.2	0.9
Average	41.9	41.4	1.4

**Table 5.** Vented design experimental and simulation temperature comparison.

Battery	Vented Experimental Model Steady State Temp °C	Vented Simulation Model Temp °C	Absolute Error Temp °C
1	33.6	36.1	2.4
2	32.9	33.7	0.8
3	33.3	32.4	0.9
4	32.2	29.7	2.5
5	33.9	37	3.05
6	32.9	33.7	0.8
7	31.8	32.6	0.8
8	31.2	30.8	0.4
9	44.2	46.6	2.4
10	43.1	46	2.9
11	44.1	45	0.9
12	42.2	41	1.2
13	45.9	49	3.1
14	44.3	44.1	0.23
15	45.3	45	1.28
16	43.8	42	1.8
Average	38.4	39.0	1.53

Differences in temperatures between simulation and experiment did not exceed 3.1 °C (battery 9), with an average difference of 1.4 °C for the default model and a mean error of 1.5 °C for the vented model. Battery 9 is situated on the top rack, front side. From Figure 12, it is seen that the air was accelerated to the back, and that batteries at the back on the lower rack were cooled better, while those on the top rack, front side, were less affected by the cooling air.

To visualize the comparison of these validation temperatures, Figures 13 and 14 show battery temperatures for the default and vented model, respectively. Both figures show that the temperature trends for each branch of the circuit followed the same profile seen in experiment. For example, the large temperature difference between battery on the upper and lower levels of the vented model was observed within simulation.

**Figure 13.** Comparison of experimental steady state temperatures against the simulation temperatures for the default design.

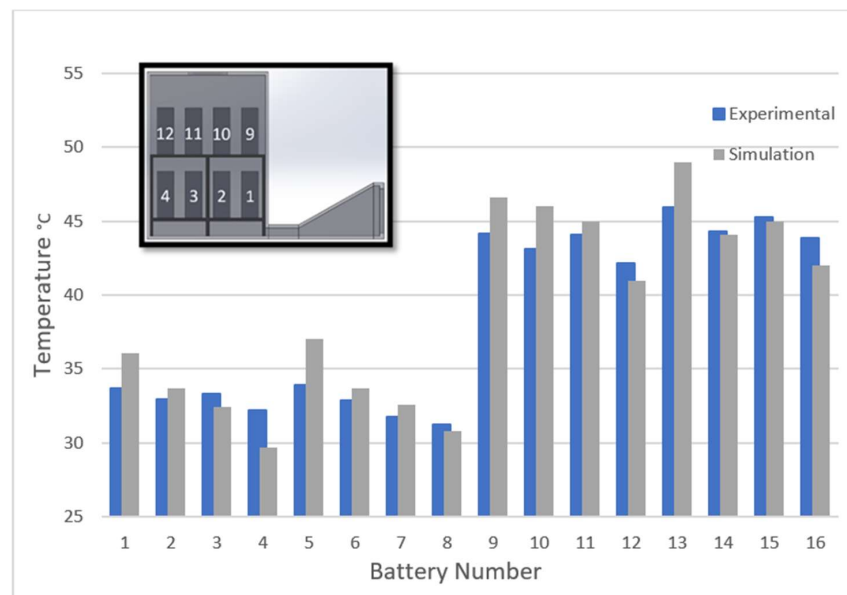


**Figure 14.** Comparison of experimental steady state temperatures against the simulation temperatures for the vented design.

Discrepancies between experimental and simulation results may have arisen from a number of different sources. A source of error is suspected to lie in the fact that the inlet air flow was undeveloped within the experimental model due to the proximity to the fan air inlet (i.e., due to system effect). Another source of error may come from the battery heat generation model used. Only resistive heating was accounted for in describing the volumetric heat generation per battery. While this is assumed to be the dominant source of heat generation for lead-acid batteries at high discharge rates, reversible heat generation is present and does have an effect on total heat generated. Another simplifying assumption was identical and constant internal resistance for each battery. In reality, internal resistance can change with battery temperature and state of charge. In summary, CFD simulation was able to predict battery temperatures reasonably well for both the vented and default designs. The average absolute difference for both models was less than 2 °C; perhaps more importantly the overall trends in battery temperature were followed.

#### 4.2. Full-Scale Simulation

Following the validation study, analysis for the full-size design was performed. Battery temperatures predicted through the full-scale simulation are listed in Table 6. Based on these temperatures, the vented model provided a reduction in average battery temperature of nearly 5 °C in comparison to the default model. In addition, no battery exceeded a temperature of 40 °C within the vented model. Analysis of the resulting battery heating trends was done by plotting temperatures, as seen in Figure 15.

From Figure 15, it can be observed that large temperature imbalances exist along the battery series 1–4, 5–8, 9–12, and 13–16 for the default model and vortex generator model. Temperature differentials for each of the battery series can be seen in Table 7. As stated within the literature review section, ASHRAE/IEEE standards stipulate that temperature differentials of more than 3 °C between batteries in series should be avoided. For the default model, the highest temperature differential of 14.4 °C occurred in battery series 13–16. In comparison, the maximum battery differential seen in the vented model was 4.1 °C. It is worth mentioning, while the vortex generator (VG) model did experience high temperature differentials for nearly all battery series; this effect was reduced in comparison to the default model.

**Table 6.** Battery simulation temperatures for the full-scale default, vented, and vortex generator cooling design models.

Battery	Default Model Temp (°C)	Vented Model Temp (°C)	Vortex Generator Model Temp (°C)
1	41.5	27	38.5
2	36.6	26.3	35.7
3	30.9	25.8	31.7
4	28.7	25.4	27.3
5	40.5	26.9	40.4
6	36	26.8	35.6
7	30.9	25.6	29.9
8	28	25.4	27.6
9	44.6	35.1	38.7
10	34	32.9	33.6
11	32.2	31	30.1
12	31.2	32.7	28
13	44.4	34.7	40.7
14	34.1	33.5	33.3
15	31	30.8	29.7
16	30	32.7	28.3
Average:	34.7	29.5	33.1

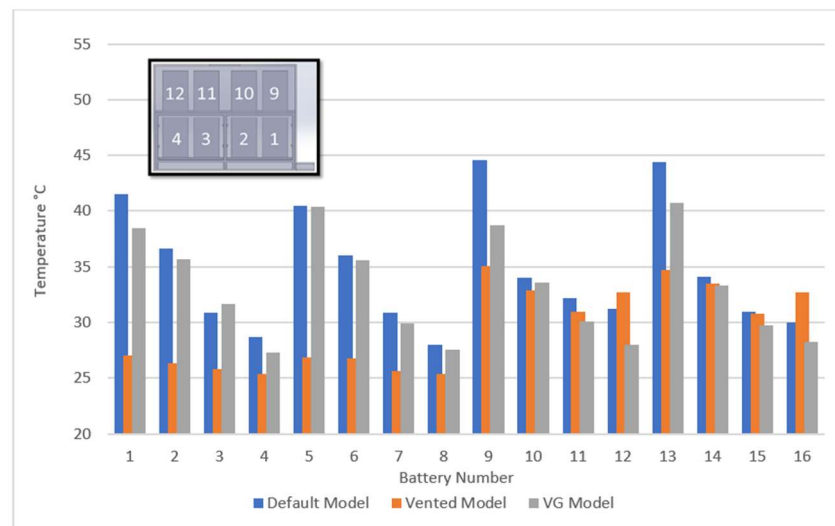


**Figure 15.** Battery temperature profiles plotted according to assigned number. The pattern for numerical labeling shown in the top right corner repeats for the other side of the case with 9–12 on the lower level of the rack and 13–16 on the top level.

**Table 7.** Temperature differentials across battery series for each of the three models.

Battery Series	Default Model Temperature Differentials (°C)	Vented Model Temperature Differentials (°C)	Vortex Generator Temperature Differentials (°C)
1–4	12.8	1.6	11.2
5–8	12.5	1.5	12.8
9–12	13.4	4.1	10.7
13–16	14.4	3.9	12.4
Average:	13.2	2.7	11.7

Visualizations of air flow through each of the designs can be seen in Figures 16–22, where air velocity is plotted. Inspecting these flow profiles yields insight into the physical processes behind the temperature profiles previously given in the Tables. The default

model is displayed in Figure 16 and shows that most of the inlet air flow is not effectively and uniformly distributed in the enclosure. This gives explanation to the trend of high battery temperature differentials experienced for cells in series, which can be seen visually in Figure 17.

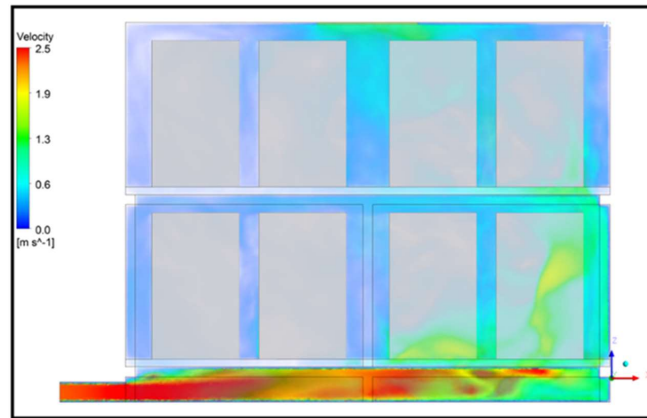


**Figure 16.** Air flow profile for the default model. Notice that batteries opposite the inlet receive the majority of air flow.

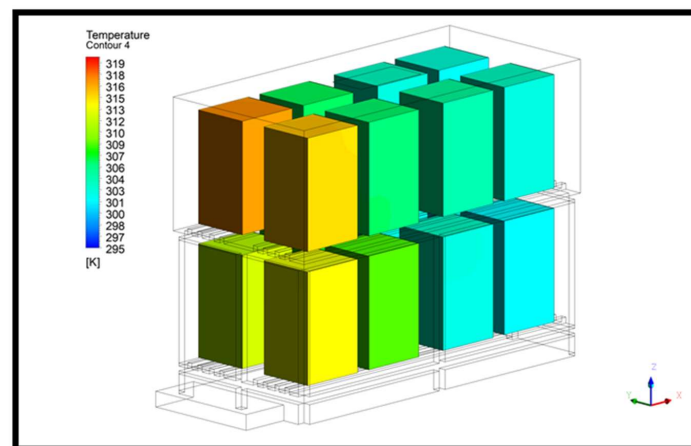


**Figure 17.** Default model battery temperatures resulting from simulation.

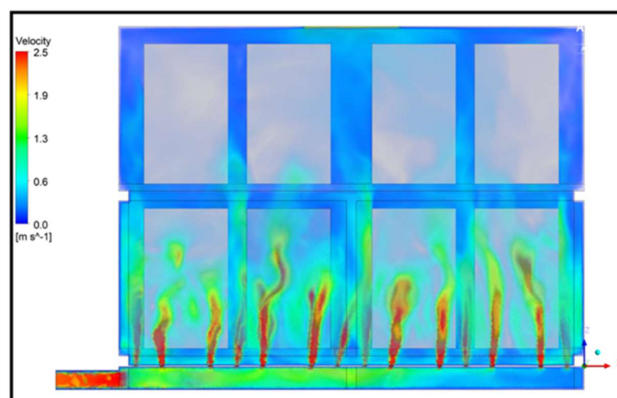


**Figure 18.** Air flow profile for the vented cooling design. An improved distribution of air can be seen in comparison to the profile shown in Figure 15.

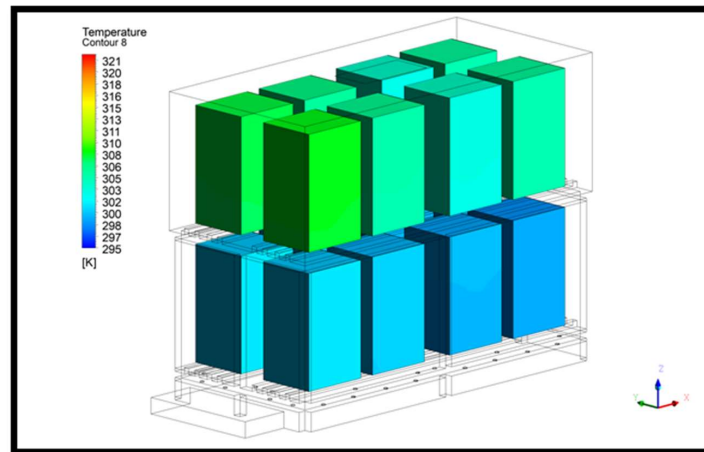


Figure 19. Vented model battery temperatures resulting from simulation.

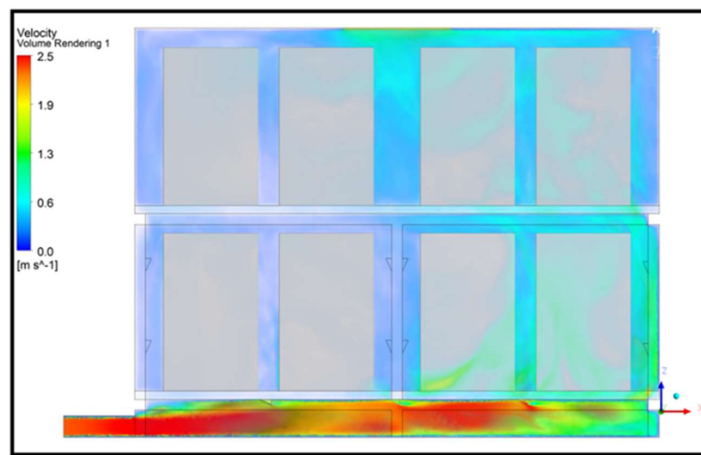


Figure 20. Air flow profile for the vortex generator design.

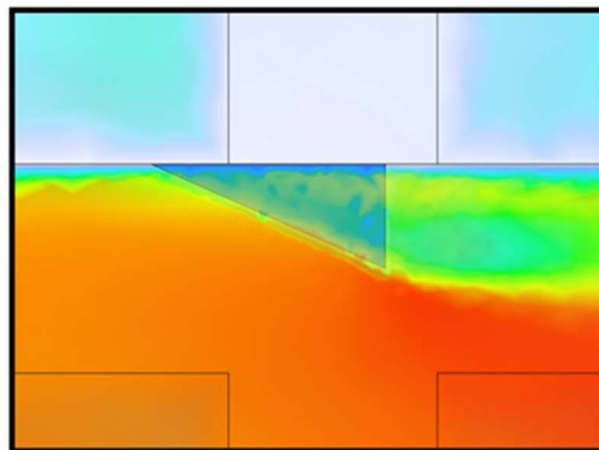


Figure 21. Vortex generator attached to the bottom of the rack. The boundary layer disruption and wake can be seen trailing the feature.

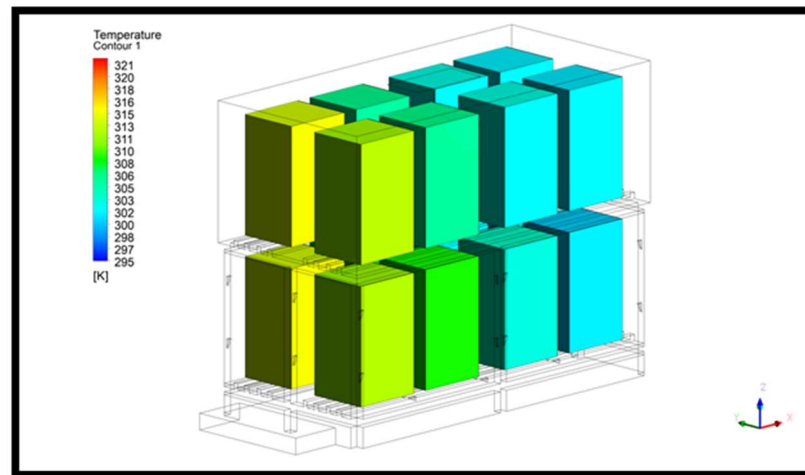


Figure 22. Vortex generator model battery temperatures resulting from simulation.

The vented model flow profile is seen in Figure 18; the resulting battery temperatures can be seen in Figure 19. Air flow distribution was improved in this design with jets of air present on each side of the battery. Additionally, these air jets have high velocity increasing the convective cooling at fluid/solid interfaces. The average battery temperature for the vented model is reduced by approximately 5.2 °C, with the greatest reduction in temperature occurring for batteries close to the inlet. The improved distribution of air is responsible for the reduction in overall temperature and the promotion of temperature uniformity among batteries as shown in Figure 19.

The model employing vortex generators, shown in Figure 20, experienced a decrease in temperature for nearly each battery in comparison to the default model. The most dramatic temperature reductions were for batteries 9 and 13 on the top rack, with each battery experiencing approximately 5 °C decrease in temperature. The battery temperatures are shown in Figure 22. The disruption of flow caused by Vortex Generators was believed to have improved the air flow distribution within the enclosure. This can be seen in Figure 21, where the flow disruption of a vortex generator mounted to the bottom of the rack is shown.

Using Ansys software and the process outlined in Section 3.5, an average Nusselt number ( $Nu$ ) at the fluid-solid boundary for each of the batteries was derived.  $Nu$  increases with heat transfer via convection; thus, it is expected that higher  $Nu$  values will result in increased cooling and lower temperatures. All values derived from  $Nu$  are averages over the side walls of individual batteries. The derived average surface  $Nu$  values have been plotted with temperature in Figure 23.

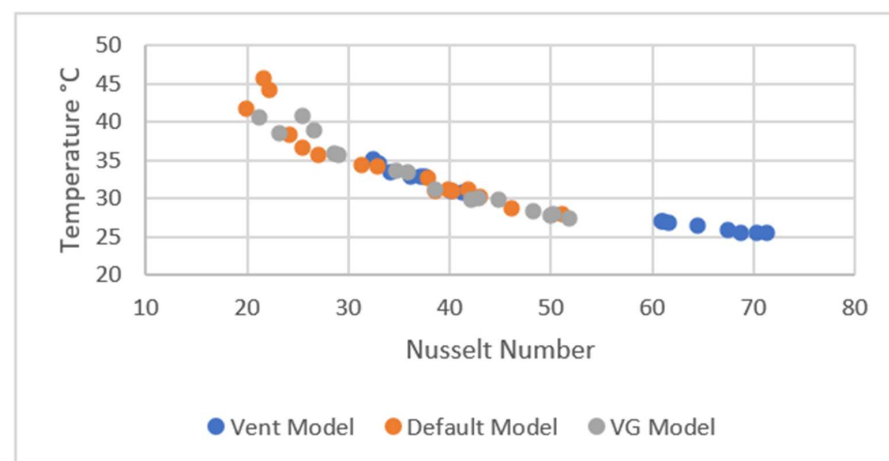


Figure 23. Battery temperature plotted as a function of the average local Nusselt number.

Figure 23 shows that there was a clear relationship between  $Nu$  and the resulting temperature. As convection is the only method of cooling in simulation, this is an expected result. Average  $Nu$  values between the default and vortex generator models were calculated to be 33 and 37, respectively. This result suggests that the vortex generators resulted in the intended effect to increase mixing and cooling within the battery case.

## 5. Conclusions

The research investigated potential methods for improving cooling efficiency for stationary batteries. From the simulation, it can be concluded that both vortex generator and vented models showed enhanced cooling performances. Use of components to evenly distribute airflow and disrupt flow show promise as effective methods for lowering battery temperatures without increasing inlet air flow or lowering inlet air temperature. By analyzing the cooling performance for the vented design, it is clear that components meant to increase air mixing will yield beneficial results in cooling and in increasing temperature uniformity. Not only is the average battery temperature for the vented model drastically reduced, the magnitude of temperature differentials also decreased. Combined, these effects will extend battery cycle life and reduce costs associated with replacing faulty batteries. The energy used in cooling the batteries was also reduced. Future work could focus on investigating the combined performance of vortex generator and vented models.

**Author Contributions:** G.H.: Supervising, conceptualization, paper writing; T.P.: experimental design, M.H.: MSME student. All authors have read and agreed to the published version of the manuscript.

**Funding:** This research was partly supported by the ConocoPhillips Arctic Science and Engineering Endowment Award and the ASHRAE Undergraduate Program Equipment Grants Program.

**Institutional Review Board Statement:** Not applicable.

**Informed Consent Statement:** Not applicable.

**Conflicts of Interest:** The authors declare no conflict of interest.

## References

1. Kreith, F. *Principles of Sustainable Energy Systems*, 2nd ed.; CRC Press: Boca Raton, FL, USA, 2013.
2. Xia, G.; Cao, L.; Bi, G. A review on battery thermal management in electric vehicle application. *J. Power Sources* **2017**, *367*, 90–105. [[CrossRef](#)]
3. Kim, J.; Oh, J.; Lee, H. Review on battery thermal management system for electric vehicles. *J. Appl. Therm. Eng.* **2019**, *149*, 192–212. [[CrossRef](#)]
4. Hammond, R.; Everingham, S.; Srinivasan, D. Batteries for Stationary Standby and for Stationary Cycling Applications Part 1: Standby vs. Cycling—Definitions and Concepts. In Proceedings of the IEEE Power Engineering Society General Meeting (IEEE Cat. No.03CH37491), Toronto, ON, Canada, 13–17 July 2003; pp. 141–145. [[CrossRef](#)]
5. Amrouche, S.O.; Rekioua, D.; Rekioua, T.; Bacha, S. Overview of energy storage in renewable energy systems. *Int. J. Hydrog. Energy* **2016**, *41*, 20914–20927. [[CrossRef](#)]
6. Divya, K.C.; Østergaard, J. Battery energy storage technology for power systems—An overview. *Electr. Power Syst. Res.* **2009**, *79*, 511–520. [[CrossRef](#)]
7. Barton, J.P.; Infield, D.G. Energy Storage and Its Use With Intermittent Renewable Energy. *IEEE Trans. Energy Convers.* **2004**, *19*, 441–448. [[CrossRef](#)]
8. Nor, N.M.; Ali, A.; Ibrahim, T.; Romlie, M.F. Battery Storage for the Utility-Scale Distributed Photovoltaic Generations. *IEEE Access* **2018**, *6*, 1137–1154. [[CrossRef](#)]
9. Yang, Z.; Liu, J.; Baskaran, S.; Imhoff, C.H.; Holladay, J.D. Enabling renewable energy—And the future grid—With advanced electricity storage. *JOM* **2010**, *62*, 14–23. [[CrossRef](#)]
10. Hu, X.; Zou, C.; Zhang, C.; Li, Y. Technological Developments in Batteries: A Survey of Principal Roles, Types, and Management Needs. *IEEE Power Energy Mag.* **2017**, *15*, 20–31. [[CrossRef](#)]
11. Lawder, M.T.; Suthar, B.; Northrop, P.W.C.; De, S.; Hoff, C.M.; Leitermann, O.; Crow, M.L.; Santhanagopalan, S.; Subramanian, V.R. Battery Energy Storage System (BESS) and Battery Management System (BMS) for Grid-Scale Applications. *Proc. IEEE* **2014**, *102*, 1014–1030. [[CrossRef](#)]
12. McKeon, B.B.; Furukawa, J.; Fenstermacher, S. Advanced Lead–Acid Batteries and the Development of Grid-Scale Energy Storage Systems. *Proc. IEEE* **2014**, *102*, 951–963. [[CrossRef](#)]

13. LaCommare, K.; Eto, J. Cost of power interruptions to electricity consumers in the United States (US). *Energy* **2006**, *31*, 1845–1855. [[CrossRef](#)]
14. Neacșu, D.O. *Telecom Power Systems*; CRC Press: Boca Raton, FL, USA, 2017.
15. Ferraro, M.; Brunaccini, G.; Sergi, F.; Aloisio, D.; Randazzo, N.; Antonucci, V. From Uninterruptible Power Supply to resilient smart micro grid: The case of a battery storage at telecommunication station. *J. Energy Storage* **2020**, *28*, 101207. [[CrossRef](#)]
16. Telaretti, E.; Dusonchet, L. Stationary battery technologies in the U.S.: Development Trends and prospects. *Renew. Sustain. Energy Rev.* **2017**, *75*, 380–392. [[CrossRef](#)]
17. Corey, G. Batteries for Stationary Standby and for Stationary Cycling Applications Part 6: Alternative Electricity Storage Technologies. In Proceedings of the IEEE Power Engineering Society General Meeting (IEEE Cat. No.03CH37491), Toronto, ON, Canada, 13–17 July 2003; pp. 164–169. [[CrossRef](#)]
18. Schainker, R. Executive Overview: Energy Storage Options for A Sustainable Energy Future. In Proceedings of the IEEE Power Engineering Society General Meeting, Denver, CO, USA, 6–10 June 2004; pp. 2309–2314. [[CrossRef](#)]
19. Ruetschi, P. Aging mechanisms and service life of lead–acid batteries. *J. Power Sources* **2004**, *127*, 33–44. [[CrossRef](#)]
20. Smith, K.; Saxon, A.; Keyser, M.; Lundstrom, B.; Cao, Z.; Roc, A. Life prediction model for grid-connected Li-ion battery energy storage system. In Proceedings of the American Control Conference (ACC), Seattle, WA, USA, 24–26 May 2017; pp. 4062–4068. [[CrossRef](#)]
21. Leng, F.; Tan, C.M.; Pecht, M. Effect of Temperature on the Aging rate of Li Ion Battery Operating above Room Temperature. *Sci. Rep.* **2015**, *5*, 12967. [[CrossRef](#)] [[PubMed](#)]
22. Rao, Z.; Wang, S. A review of power battery thermal energy management. *Renew. Sustain. Energy Rev.* **2011**, *15*, 4554–4571. [[CrossRef](#)]
23. Liu, L.; Sun, H.; Li, C.; Li, T.; Xin, J.; Zheng, N. Managing Battery Aging for High Energy Availability in Green Datacenters. *IEEE Trans. Parallel Distrib. Syst.* **2017**, *28*, 3521–3536. [[CrossRef](#)]
24. Stan, A.-I.; Swierczynski, M.J.; Stroe, D.-I.; Teodorescu, R.; Andreassen, S.J.; Moth, K. A Comparative Study of Lithium Ion to Lead Acid Batteries for Use in UPS Applications. In Proceedings of the IEEE 36th International Telecommunications Energy Conference (IN<sup>TEL</sup>EC), Vancouver, BC, Canada, 28 September–2 October 2014. [[CrossRef](#)]
25. Santhanagopalan, S.; Smith, K.; Neubauer, J. *Design and Analysis of Large Lithium-Ion Battery Systems*; Artech: Norwood, MA, USA, 2014.
26. Hesse, H.C.; Schimpe, M.; Kucevic, D.; Jossen, A. Lithium-Ion Battery Storage for the Grid—A Review of Stationary Battery Storage System Design Tailored for Applications in Modern Power Grids. *Energies* **2017**, *10*, 2107. [[CrossRef](#)]
27. *1187-2013*; IEEE Recommended Practice for Installation Design and Installation of Valve-Regulated Lead-Acid Batteries for Stationary Applications; IEEE Std 1187-2013 Revis. IEEE Std 1187-2002. IEEE: New York, NY, USA, 2014. [[CrossRef](#)]
28. IEEE/ASHRAE. *Guide for the Ventilation and Thermal Management of Batteries for Stationary Applications*; IEEE Std 1635-2012ASHRAE Guidel. 21-2012; IEEE: New York, NY, USA, 2012; pp. 1–108. [[CrossRef](#)]
29. Jouhara, H.; Khordehghah, N.; Serey, N.; Almahmoud, S.; Lester, S.P.; Machen, D.; Wrobel, L. Applications and thermal management of rechargeable batteries for industrial applications. *Energy* **2019**, *170*, 849–861. [[CrossRef](#)]
30. Chiu, K.-C.; Lin, C.-H.; Yeh, S.-F.; Lin, Y.-H.; Huang, C.-S.; Chen, K.-C. Cycle life analysis of series connected lithium-ion batteries with temperature difference. *J. Power Sources* **2014**, *263*, 75–84. [[CrossRef](#)]
31. Hart, D.; Sarkissian, A. *Deployment of Grid-Scale Batteries in the United States*; U.S. Department of Energy: Washington, DC, USA, 2016; p. 31.
32. Kosik, B. ASHRAE’s Energy Standard for Data Centers Turns Three. *CSE* **2019**, *56*, 24–30.
33. Zhang, H.; Shao, S.; Xu, H.; Zou, H.; Tian, C. Free cooling of data centers: A review. *Renew. Sustain. Energy Rev.* **2014**, *35*, 171–182. [[CrossRef](#)]
34. Daraghmeh, H.M.; Wang, C.-C. A review of current status of free cooling in datacenters. *Appl. Therm. Eng.* **2017**, *114*, 1224–1239. [[CrossRef](#)]
35. Mohammadian, S.K.; He, Y.-L.; Zhang, Y. Internal cooling of a lithium-ion battery using electrolyte as coolant through microchannels embedded inside the electrodes. *J. Power Sources* **2015**, *293*, 458–466. [[CrossRef](#)]
36. Jaguemont, J.; Van Mierlo, J. A comprehensive review of future thermal management systems for battery-electrified vehicles. *J. Energy Storage* **2020**, *31*, 101551. [[CrossRef](#)]
37. Buidin, T.I.C.; Mariasiu, F. Battery thermal management systems: Current status and design approach of cooling technologies. *Energies* **2021**, *14*, 4879. [[CrossRef](#)]
38. Spitthoff, L.; Shearing, P.; Burheim, O. Temperature, Ageing and Thermal Management of Lithium-Ion Batteries. *Energies* **2021**, *14*, 1248. [[CrossRef](#)]
39. Jeffs, J.; Dinh, T.Q.; Widanage, W.D.; McGordon, A.; Picarelli, A. Optimisation of Direct Battery Thermal Management for EVs Operating in Low-Temperature Climates. *Energies* **2020**, *13*, 5980. [[CrossRef](#)]
40. Akinlabi, A.H.; Solyali, D. Configuration, design, and optimization of air-cooled battery thermal management system for electric vehicles: A review. *Renew. Sustain. Energy Rev.* **2020**, *125*, 109815. [[CrossRef](#)]
41. Chen, K.; Chen, Y.; She, Y.; Song, M.; Wang, S.; Chen, L. Construction of effective symmetrical air-cooled system for battery thermal management. *Appl. Therm. Eng.* **2019**, *166*, 114679. [[CrossRef](#)]
42. Monika, K.; Chakraborty, C.; Roy, S.; Dinda, S.; Singh, S.A.; Datta, S.P. An improved mini-channel based liquid cooling strategy of prismatic LiFePO<sub>4</sub> batteries for electric or hybrid vehicles. *J. Energy Storage* **2021**, *35*, 102301. [[CrossRef](#)]

43. Dubey, P.; Pulugundla, G.; Srouji, A. Direct Comparison of Immersion and Cold-Plate Based Cooling for Automotive Li-Ion Battery Modules. *Energies* **2021**, *14*, 1259. [CrossRef]
44. Gschwander, S.; Niedermaier, S.; Gamisch, S.; Kick, M.; Klünder, F.; Haussmann, T. Storage Capacity in Dependency of Supercooling and Cycle Stability of Different PCM Emulsions. *Appl. Sci.* **2021**, *11*, 3612. [CrossRef]
45. Wu, W.; Wang, S.; Wu, W.; Chen, K.; Hong, S.; Lai, Y. A critical review of battery thermal performance and liquid based battery thermal management. *Energy Convers. Manag.* **2019**, *182*, 262–281. [CrossRef]
46. Bandhauer, T.M.; Garimella, S.; Fuller, T.F. A Critical Review of Thermal Issues in Lithium-Ion Batteries. *J. Electrochem. Soc.* **2011**, *158*, R1. [CrossRef]
47. Khan, M.; Swierczynski, M.; Kær, S. Towards an Ultimate Battery Thermal Management System: A Review. *Batteries* **2017**, *3*, 9. [CrossRef]
48. Yang, N.; Zhang, X.; Shang, B.; Li, G. Unbalanced discharging and aging due to temperature differences among the cells in a lithium-ion battery pack with parallel combination. *J. Power Sources* **2016**, *306*, 733–741. [CrossRef]
49. Brzezińska, D. Ventilation System Influence on Hydrogen Explosion Hazards in Industrial Lead-Acid Battery Rooms. *Energies* **2018**, *11*, 2086. [CrossRef]
50. Al-Zareer, M.; Dincer, I.; Rosen, M.A. A thermal performance management system for lithium-ion battery packs. *Appl. Therm. Eng.* **2019**, *165*, 114378. [CrossRef]
51. Schmidt, R.; Shaukatullah, H. Computer and telecommunications equipment room cooling: A review of literature. *IEEE Trans. Components Packag. Technol.* **2003**, *26*, 89–98. [CrossRef]
52. Lu, H.; Zhang, Z.; Yang, L. A review on airflow distribution and management in data center. *Energy Build.* **2018**, *179*, 264–277. [CrossRef]
53. ASHRAE Technical Committee. *Data Center Power Equipment Thermal Guidelines and Best Practices*; ASHREA TC99; ASHRAE Technical Committee: Peachtree Corners, GA, USA, 2016; pp. 1–60.
54. Butler, P.; Dunleavy, J.; Farber-DeAnda, M.; Moseley, P. Performance of valve-regulated lead-acid batteries in real-world stationary applications—Utility installations. *J. Power Sources* **2001**, *96*, 94–101. [CrossRef]
55. Garche, J.; Jossen, A. Battery Management Systems (BMS) for Increasing Battery Life Time. In Proceedings of the TEL-ESCON 2000, Third International Telecommunications Energy Special Conference (IEEE Cat. No.00EX424), Dresden, Germany, 7–10 May 2000; pp. 81–88.
56. Cho, J.; Jeong, S.; Kim, Y. Commercial and research battery technologies for electrical energy storage applications. *Prog. Energy Combust. Sci.* **2015**, *48*, 84–101. [CrossRef]
57. Xie, Q.; Yue, S.; Pedram, M.; Shin, D.; Chang, N.; Qing, X. Adaptive Thermal Management for Portable System Batteries by Forced Convection Cooling. In Proceedings of the Design, Automation Test in Europe Conference Exhibition (DATE), Grenoble, France, 19–22 March 2013; pp. 1225–1228. [CrossRef]
58. He, F.; Ma, L. Thermal management of batteries employing active temperature control and reciprocating cooling flow. *Int. J. Heat Mass Transf.* **2015**, *83*, 164–172. [CrossRef]
59. Chang, G.; Cui, X.; Li, Y.; Ji, Y. Effects of reciprocating liquid flow battery thermal management system on thermal characteristics and uniformity of large lithium-ion battery pack. *Int. J. Energy Res.* **2020**, *44*, 6383–6395. [CrossRef]
60. Arasaratnam, I.; Tjong, J.; Ahmed, R.; El-Sayed, M.; Habibi, S. Adaptive Temperature Monitoring for Battery Thermal Management. In Proceedings of the IEEE Transportation Electrification Conference and Expo (ITEC), Detroit, MI, USA, 16–19 June 2013; pp. 1–6. [CrossRef]
61. Xiong, R.; Li, L.; Tian, J. Towards a smarter battery management system: A critical review on battery state of health monitoring methods. *J. Power Sources* **2018**, *405*, 18–29. [CrossRef]
62. Ali, H.A.A.; Abdeljawad, Z.N. Thermal Management Technologies of Lithium-Ion Batteries Applied for Stationary Energy Storage Systems: Investigation on the Thermal Behavior of Lithium-Ion Batteries. Master's Thesis, Mälardalens University, Västerås, Sweden, 2020.
63. Chen, D.; Jiang, J.; Kim, G.-H.; Yang, C.; Pesaran, A. Comparison of different cooling methods for lithium ion battery cells. *Appl. Therm. Eng.* **2016**, *94*, 846–854. [CrossRef]
64. Liu, H.; Wei, Z.; He, W.; Zhao, J. Thermal issues about Li-ion batteries and recent progress in battery thermal management systems: A review. *Energy Convers. Manag.* **2017**, *150*, 304–330. [CrossRef]
65. Al-Zareer, M.; Dincer, I.; Rosen, M.A. A review of novel thermal management systems for batteries. *Int. J. Energy Res.* **2018**, *42*, 3182–3205. [CrossRef]
66. Wilke, S.; Schweitzer, B.; Khateeb, S.; Al-Hallaj, S. Preventing thermal runaway propagation in lithium ion battery packs using a phase change composite material: An experimental study. *J. Power Sources* **2017**, *340*, 51–59. [CrossRef]
67. Madani, S.S.; Swierczynski, M.J.; Kaer, S.K. A review of Thermal Management and Safety for Lithium Ion Batteries. In Proceedings of the Twelfth International Conference on Ecological Vehicles and Renewable Energies, Monte Carlo, Monaco, 11–13 April 2017; pp. 1–20. [CrossRef]
68. C&D Technologies. MCT-HP Data Sheet. 2020. Available online: [https://cdtechno.com/wp-content/uploads/2020/05/MCT-HP\\_DataSheet.pdf](https://cdtechno.com/wp-content/uploads/2020/05/MCT-HP_DataSheet.pdf) (accessed on 12 December 2020).
69. Bayazit, Y.; Sparrow, E.M.; Joseph, D.D. Perforated plates for fluid management: Plate geometry effects and flow regimes. *Int. J. Therm. Sci.* **2014**, *85*, 104–111. [CrossRef]

70. Ke, Z.; Chen, C.-L.; Li, K.; Wang, S.; Chen, C.-H. Vortex dynamics and heat transfer of longitudinal vortex generators in a rectangular channel. *Int. J. Heat Mass Transf.* **2018**, *132*, 871–885. [[CrossRef](#)]
71. Awais, M.; Bhuiyan, A.A. Heat transfer enhancement using different types of vortex generators (VGs): A review on experimental and numerical activities. *Therm. Sci. Eng. Prog.* **2018**, *5*, 524–545. [[CrossRef](#)]
72. Saw, B.; Ye, Y.; Tay, A.A.; Chong, W.T.; Kuan, S.H.; Yew, M.C. Computational fluid dynamic and thermal analysis of Lithium-ion battery pack with air cooling. *Appl. Energy* **2016**, *177*, 783–792. [[CrossRef](#)]
73. Alonzo-García, A.; del Carmen Gutiérrez-Torres, C.; Jiménez-Bernal, J.A. Computational Fluid Dynamics in Turbulent Flow Applications. *Life Sci.* **2016**. [[CrossRef](#)]
74. Ahn, J.; Sparrow, E.; Gorman, J. Turbulence intensity effects on heat transfer and fluid-flow for a circular cylinder in crossflow. *Int. J. Heat Mass Transf.* **2017**, *113*, 613–621. [[CrossRef](#)]
75. Wanko Tchatchouang, C. *Effects of Turbulence Modeling in Predicting Flow and Heat Transfer in a Duct with Pin Fins*; Purdue University: West Lafayette, IN, USA, 2012.
76. Freund, S.; Kabelac, S. Investigation of local heat transfer coefficients in plate heat exchangers with temperature oscillation IR thermography and CFD. *Int. J. Heat Mass Transf.* **2010**, *53*, 3764–3781. [[CrossRef](#)]
77. Li, W.H.; Ren, J.; Jiang, H.D.; Luan, Y.G.; Ligrani, P. Assessment of six turbulence models for modeling and predicting narrow passage flows, part 2: Pin fin arrays. *Numer. Heat Transf. Part A Appl.* **2016**, *69*, 445–463. [[CrossRef](#)]
78. Shabani, B.; Biju, M. Theoretical Modelling Methods for Thermal Management of Batteries. *Energies* **2015**, *8*, 10153–10177. [[CrossRef](#)]
79. Shen, M.; Gao, Q. A review on battery management system from the modeling efforts to its multiapplication and integration. *Int. J. Energy Res.* **2019**, *43*, 5042–5075. [[CrossRef](#)]
80. Cengel, Y. *Heat and Mass Transfer: Fundamentals and Applications*; McGraw-Hill Higher Education: New York, NY, USA, 2014.
81. Choi, K.W.; Yao, N.P. *Engineering Analysis of Thermal Phenomena for Lead—Acid Batteries during Recharge Processes*; Argonne National Lab. (ANL): Argonne, IL, USA, 1977.
82. Al Hallaj, S.; Maleki, H.; Hong, J.; Selman, J. Thermal modeling and design considerations of lithium-ion batteries. *J. Power Sources* **1999**, *83*, 1–8. [[CrossRef](#)]
83. Moseley, P.; Rand, D.; Garche, J. *Lead—Acid Batteries for Future Automobiles*; Oxford Elsevier: Oxford, UK, 2017; pp. 601–618. [[CrossRef](#)]
84. Mahamud, R. *Advanced Battery Thermal Management for Electrical-Drive Vehicles Using Reciprocating Cooling Flow and Spatial-Resolution, Lumped-Capacitance Thermal Model*; University of Nevada: Reno, NV, USA, 2011.
85. Daud, Z.H.C.; Chrenko, D.; Dos Santos, F.; Aglzim, E.-H.; Keromnes, A.; Le Moyne, L. 3D electro-thermal modelling and experimental validation of lithium polymer-based batteries for automotive applications. *Int. J. Energy Res.* **2016**, *40*, 1144–1154. [[CrossRef](#)]
86. Pesaran, A.A. Battery thermal models for hybrid vehicle simulations. *J. Power Sources* **2002**, *110*, 377–382. [[CrossRef](#)]
87. Peng, X.; Cui, X.; Liao, X.; Garg, A. A Thermal Investigation and Optimization of an Air-Cooled Lithium-Ion Battery Pack. *Energies* **2020**, *13*, 2956. [[CrossRef](#)]
88. Shahid, S.; Agelin-Chaab, M. Experimental and numerical studies on air cooling and temperature uniformity in a battery pack. *Int. J. Energy Res.* **2018**, *42*, 2246–2262. [[CrossRef](#)]
89. Soltani, M.; Berckmans, G.; Jaguemont, J.; Ronsmans, J.; Kakihara, S.; Hegazy, O.; Van Mierlo, J.; Omar, N. Three dimensional thermal model development and validation for lithium-ion capacitor module including air-cooling system. *Appl. Therm. Eng.* **2019**, *153*, 264–274. [[CrossRef](#)]